UDC621.746.56:669.13/15:681.3:519.6

Development and Application of Computer Simulation Techniques for Analyzing Composition, Particle Size Distribution, and Amount of Nonmetallic Inclusions in Steel

Wataru Yamada*1 Tooru Matsumiya*1
Shigeo Fukumoto*1 Masami Wajima*2
Hiroyuki Tanaka*3

Abstract:

Various simulators were developed for predicting the composition, particle size distribution, and amount of nonmetallic inclusions in steel. The simulators used for analyzing the composition of nonmetallic inclusions can predict the composition of nonmetallic inclusions remaining in continuously cast steel by coupling the analysis of various equilibria with the analysis of solute element microsegregation in the molten steel being solidified as well as the analysis of the equilibrium precipitation of nonmetallic inclusions in the residual molten steel. The simulators used for analyzing particle size distribution and the amount of nonmetallic inclusions can analyze the reactions taking place in the deoxidation process and analyze the coagulation, flotation, and removal behavior of nonmetallic inclusions occurring during continuous casting . In this paper, these analytical techniques are outlined, the composition control of inclusions in stainless steel and the conditions for the precipitation of harmful olivine inclusions are discussed, and the results obtained when these techniques were applied to the analysis of the coagulation, flotation, and removal of Al_2O_3 inclusions in the tundish of a continuous caster are reported.

1. Introduction

Nonmetallic inclusions in steel become surface defects in steel sheets, degrade the antifatigue properties of high-strength steel, and clog nozzles used in continuous casting. For these reasons, measures are taken to remove nonmetallic inclusions in the molten steel stage as much as possible. With a continuous caster tundish, for example, ceramic filters and refractory dams and weirs have been installed to promote the removal of nonmetallic inclusions from molten steel. In recent years, tundishes have increased in geometrical complexity, and electromagnetic forces have been applied to accelerate the removal of nonmetallic inclusions in them. These circumstances have called for simulation models that can quantitatively and comprehensively grasp the behavior of nonmetallic inclusions in the tundish. High-carbon

*1 Technical Development Bureau
*2 Presently Nittetu Hokkaido Control System Co.
*3 Yawata Works

high-strength steels, one of which is used as automobile tire cord steel, are sensitive to small amounts of residual nonmetallic inclusions. The compositional control of such nonmetallic inclusions is therefore an important issue. As users have increasingly imposed severe nonmetallic inclusion limits and demanded steels of increasing strength in recent years, the compositional control of nonmetallic inclusions is expected to increase in importance. This trend in turn has boosted the need for the development of techniques for predicting and controlling the composition of inclusions in steel.

Based on the development of a thermodynamic slag model[1] and the accumulation of thermodynamic equilibrium computational techniques between multiple-component systems and multiple phases[2], Nippon Steel's Advanced Technology Research Laboratories developed a simulator for analyzing the composition of nonmetallic inclusions in carbon steel[3]. The simulator can quantitatively determine the composition of nonmetallic inclusions in carbon steel after continuous casting if the chemical composition of the carbon steel after secondary refining is known. In this way, guidelines for optimizing the chemical design and refining treatment of steels for the purpose of rendering their nonmetallic inclusions harmless can be established beforehand by computation. In the present study, the simulator's scope of application was expanded to include stainless steel as well. To date, modeled reactions include the formation of nonmetallic inclusions in the deoxidation process during refining treatment, coagulation and coalescence of nonmetallic inclusions in refining vessels, reaction between the flux and molten steel during flux treatment, impingement of nonmetallic inclusions on the ladle wall, flotation of nonmetallic inclusions to the bath surface, and removal of nonmetallic inclusions from the bath surface. The outcome of these efforts was the development of a "deoxidation process simulator" for predicting the final composition, particle size distribution, and amount of nonmetallic inclusions that arise during the steel refining process. This report outlines these analytical techniques, discusses the compositional control of inclusions in stainless steel and the conditions for the precipitation of harmful olivine inclusions in stainless steel, and presents the results obtained when the deoxidation process simulator analyzed coagulation, flotation, and removal of Al_2O_3 inclusions from a continuous caster tundish.

2. Analysis of Nonmetallic Inclusion Composition in Continuously Cast Slabs of Stainless Steel[4]

Fig. 1 schematically illustrates the simulation model used to predict the compositional change of nonmetallic inclusions in carbon steel during solidification that was published in a previous report[3]. Although its details are omitted here, the model consists of the following basic steps:

1) The residual molten steel during solidification is supposed to be completely mixed, and solute diffusion in the solid phase is partially considered.
2) Thermodynamic equilibrium holds between the solute and nonmetallic inclusions in the molten steel.
3) The precipitates are trapped into the solid phase in proportion to the solid fraction and no longer play any part in further reaction.

The fundamental treatment of **Fig. 1** is also effective for high-alloyed steels like stainless steels, but the technique used for carbon steel cannot be directly applied to stainless steel containing high concentrations of nickel and chromium. The change in the solid-liquid equilibrium partition coefficient of solute elements during solidification cannot be ignored, and the information of the equilibrium partition coefficient is required for specific solidification paths. Another difficulty is the incomplete accumulation of basic thermodynamic properties for stainless steel.

Sundman et al. calculated the solidification paths of alloys by the successive method, which involves lowering the temperature in small steps, calculating the solid-liquid equilibrium at each temperature step by THERMO-CALC[5], precipitating the solid in equilibrium with the residual molten steel, and tracing the composition of the freshly formed residual molten steel,as shown in **Fig.2**[6] This technique is the same as Scheil[7] employed for handling segregation computation when it is assumed that the residual molten steel on solidification is completely mixed and that there is no solute diffusion in the solid phase. The present authors improved the technique of Sundman et al., incorporated the solute diffusion in the solid phase according to the Clyne-Kurz model[8], and applied the improved technique to the solidification path analysis of stainless steel. The partial solidification time (t_s) required as the input condition was calculated for each solid fraction from the known cooling rate (CR) by Eq. (l).

$$t_s(f_s = f_s) = \Delta T/\Delta f_s/CR \quad \cdots\cdots(1)$$

The secondary dendrite arm spacing (γ_d) was also calculated from the cooling rate by Eq. (2)[9].

$$\gamma_d = 111.3 \times CR^{0.45}\ (\mu m) \quad \cdots\cdots(2)$$

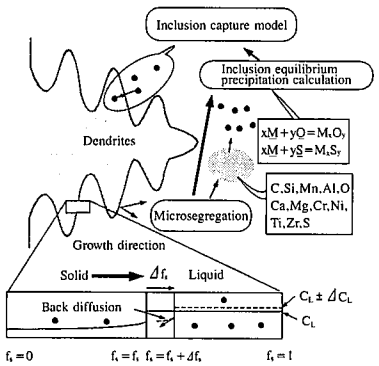

Fig. 1 Model for analyzing composition of nonmetallic inclusions in carbon steel[3]

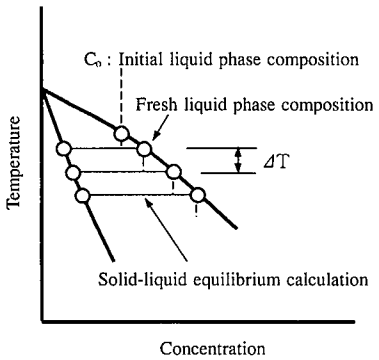

Fig. 2 Successive calculation method for solidification path by using THERMO-CALC

Concerning the thermodynamics data of alloys, the activities of constituent elements were calculated by the combination of the sublattice model of Hillert et al.[10] and the extended dilute solution approximation model of Pelton et al.[11]. These were performed to consider simultaneously the main elements such as chromium and nickel and the microalloying elements like silicon, calcium, and oxygen,respectively. The trapping of nonmetallic inclusions into the solid phase was handled differently from carbon steel. In other words, the nonmetallic inclusions were assumed not to be trapped into the solid phase in proportion to the solid fraction, but to exist as lumps of finite size and were incorporated together into the solid phase at a critical solid fraction.

Table 1 shows the chemical composition of the stainless steel wire rod used to analyze the composition of inclusions using the above-mentioned model. To prevent wire breakage during the drawing of this grade, the hard crystal phases, such as $MgO \cdot Al_2O_3$ and Al_2O_3, must be prevented from precipitating, and the melting point of the inclusions must be loweved. **Figs. 3(a)** to **3(d)** show the calculated compositions of inclusions when the oxygen content was 40, 80, 100, and 150 ppm, respectively. To minimize the amount of nonmetallic inclusions formed, the production of the tire cord steel initially focused on a low-oxygen content of about 40 ppm. As shown in **Fig. 3(a)**, when the oxygen content was reduced to 40 ppm, the Al_2O_3 concentration in nonmetallic inclusions increased and there was the great possibility that hard crystal phases, such as $MgO \cdot Al_2O_3$ and Al_2O_3, readily precipitate. As the oxygen content was increased, oxides such as SiO_2 and MnO, actually increased in concentration to raise the number of components present in the nonmetallic inclusions. **Figs. 4(a)** and **4(b)** respectively show the calculated and measured effects of the oxygen content on the Al_2O_3 and SiO_2 concentrations of the nonmetallic inclusions. If the inclusions are assumed to be entrapped into the solid phase when the solid fraction of the steel reaches 0.5, the calculated Al_2O_3 and SiO_2 concentrations agree with the measured Al_2O_3 and SiO_2 concentrations, respectively. The inclusion composition at $f_s = 0.5$ in **Fig. 3** was taken as the inclusion composition of each cast slab, and a phase diagram calculation was performed to see which oxide crystal phase would precipitate at the composition. The results are shown in **Figs. 5(a)** to **5(d)**. When the oxygen content was 40 ppm, $MgO \cdot Al_2O_3$ and Al_2O_3 both precipitate as nonmetallic inclusions in the steel when cooled. At the other oxygen contents, these hard crystal phases did not precipitate. When the oxygen content was 40 ppm, the liquidus temperature was very high at 1,767°C as predicted, because the spinel phase precipitates at high temperatures. At the higher oxygen contents, the precipitation of Cr_2O_3, a high-melting point oxide, prevented the liquidus temperature from falling appreciably. As can be seen from **Fig. 5**, the proportion of the phases to precipitate is limited to 20% or less at 1,200 to 1,330°C, the typical temperature range of wire rod steel reheating furnaces. This means that the tire cord steel retains enough workability for rolling.

The total amount of nonmetallic inclusions naturally increases with rising oxygen content. **Fig. 6** shows the calculated oxygen content dependence of the amount of nonmetallic inclusions formed. From this figure, it is clear that the precipitation of inclusions increases in approximate proportion to the increase in the oxygen content. From these results, it can be said that the optimum oxygen content for avoiding the precipitation of hard crystal phases, such as $MgO \cdot Al_2O_3$ and Al_2O_3, and for minimizing nonmetallic inclusions is about 80 ppm. This analytical finding is being put to effective use in the compositional design of stainless steel wire rods at Nippon Steel's Hikari Works.

Table. 1 Chemical composition of stainless steel SUS304 used to analyze composition of nonmetallic inclusions[4]

(wt%)

Cr	Ni	C	Si	Mn	Al
18.3	10.35	0.02	0.5	1.1	0.0015-0.0030
O		Mo	Ca	Mg	
0.0040-0.0150		0.01	0.0005	0.0004	

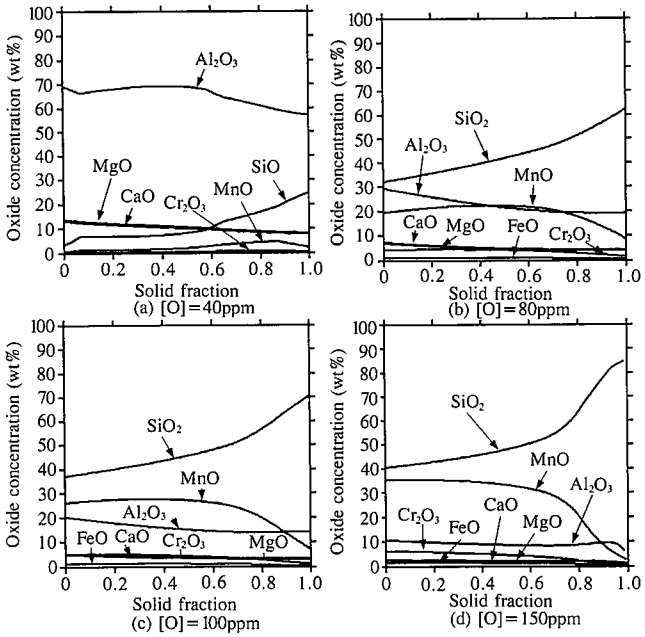

Fig. 3 Calculated changes in composition of inclusions in stainless steel SUS304 during solidification

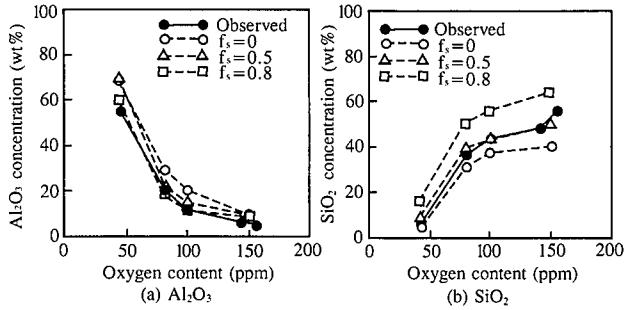

Fig. 4 Effect of oxygen content on Al_2O_3 concentration (a) and SiO_2 concentration (b) of nonmetallic inclusions

3. Evaluation of Precipitation Limit of Harmful Olivine Inclusions

In weakly deoxidized steels such as silicon-manganese deoxidized steel, magnesium pickup from refractories and the like often precipitates harmful olivine ($2MgO \cdot SiO_2$) inclusions within nonmetallic inclusions, causing the degradation of the steel's mechanical properties. Using thermodynamic model computation, this study investigated the critical MgO concentration at which the olivine precipitation can take place.

Table 2 shows the results of synthetic oxide overheating simulation experiments carried out at Nippon Steel's Muroran

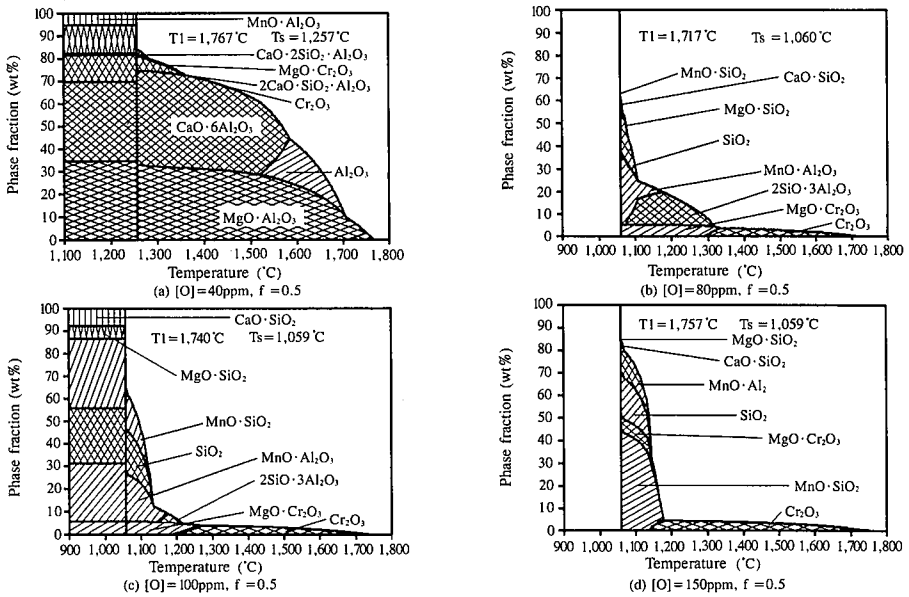

Fig. 5 Phase diagrams of nonmetallic inclusions trapped into steel at $f_s = 0.5$

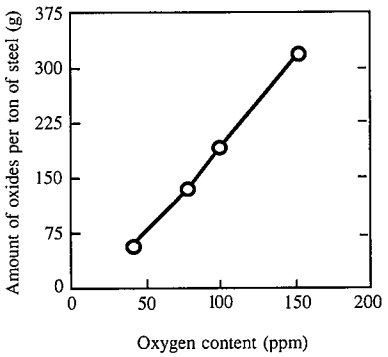

Fig. 6 Effect of oxygen content on nonmetallic inclusions in steel

Works[12] to determine the critical MgO concentration for olivine precipitation. In both which experiments where isothermal holding and thermal history, which simulated overheated furnace temperatures, were applied without modification, the precipitation of olivine crystals was observed in a high-MgO oxide (sample A). In sample B with the MgO concentration reduced to 11%, olivine did not precipitate in either experiment. It can be thus concluded that the critical MgO concentration for olivine precipitation lies in the MgO concentration range of 11 to 16%. **Fig. 7** shows the calculated temperature change of equilibrium precipitate phases in oxide A where olivine precipitation was confirmed as shown in **Table 2**. **Fig. 8** shows the olivine precipitation temperature range determined by using a metastable phase precipitation computational model on the assumption that the three oxides listed in **Table 2** precipitate crystal phases only when they assume a driving force large enough to precipitate the olivine phase as they are supercooled in the glassy state as shown in **Fig. 9**. The calculated values agree well with the measured values, and a MgO concentration of about 12% is found to be the critical MgO concentration for olivine precipitation. This finding means that the crystal

Table. 2 Results of synthetic inclusion heating experiments conducted to determine olivine precipitation conditions

Inclusion	SiO_2	CaO	Al_2O_3	MgO	MnO	Isothermal holding	Heating furnace thermal history
A	52	16	12.3	16	3.7	Precipitation at 1,200°C < T < 1,300 °C	Precipitation
B	55	17	13	11	4	No precipitation	No precipitation
C	58	18	13.7	6	4.3	No experiment	No experiment

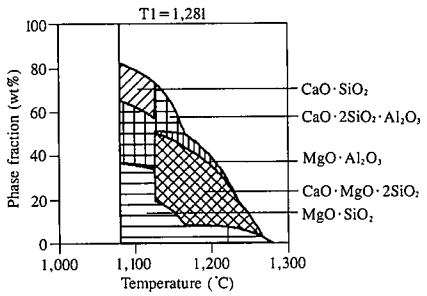

Fig. 7 Equilibrium phase diagram of inclusion A

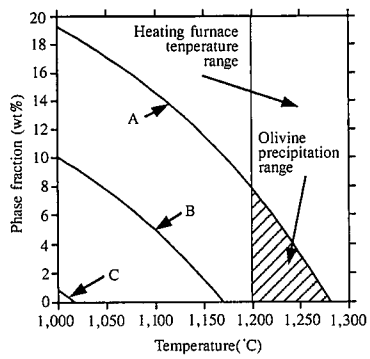

Fig. 8 Calculated amount of olivine precipitated from glass matrix

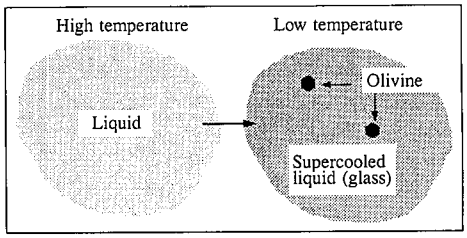

Fig. 9 Schematic illustration of olivine precipitation from glass matrix

Table. 3 Calculated chemical compositions of nonmetallic inclusions with magnesium pickup from refractories

(wt%)

No.	Level;	Mgo	SiO_2	CaO	Al_2O_3	MnO
No.1	Pickup of 1 ppm	10.9	38.9	23.0	23.0	4.2
No.2	Pickup of 1 ppm	17.9	38.8	25.1	23.2	0.0
No.3	Pickup of 3 ppm	26.7	24.1	22.5	26.6	0.1

Table. 4 Chemical composition of spring steel

(wt%)

C	Si	Mn	P	S	Al	T.O
0.58	1.35	0.70	0.015	0.005	0.001	0.0025

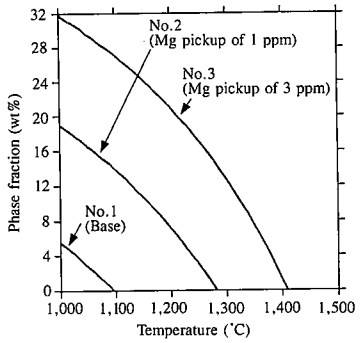

Fig. 10 Olivine precipitation curves with magnesium pickup from refractories

phase precipitation sequence of oxides that easily form glass, such as multicomponent oxides, does not always depend on their thermodynamic equilibrium conditions.

Table 3 shows the chemical compositions of inclusions calculated from thermodynamic equilibra by taking the chemical composition of the spring steel listed in **Table 4** as the base, and by assuming that the magnesium picked up from the refractories dissolves in amounts of 1 and 3 ppm when converted into the magnesium concentration in the molten steel. As evident from the calculated values in **Table 3**, the magnesium pickup from the refractories markedly increases the MgO concentration and significantly promotes olivine precipitation as shown in **Fig. 10**.

4. Development of Deoxidation Process Simulator, and Computation of Coagulation, Flotation and Removal Behavior of Nonmetallic Inclusions

Fig. 11 provides an overview of the deoxidation process simulator. The refining vessel or continuous casting tundish is divided into several spatial elements. In each spatial element, the following reactions are calculated at each step: 1) equilibrium precipitation of inclusions from molten steel; 2) slag/molten steel

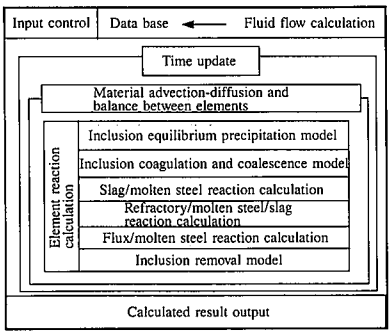

Fig. 11 System outline of deoxidation process simulator

reaction; 3) coagulation and coalescence of inclusions; 4) refractory/molten steel reaction; and 5) refining flux/molten steel reaction. The advection of the molten steel and inclusions between the spatial elements is calculated and balanced by considering the flotation of the inclusions. This series of calculations is repeated with time to predict the final composition, amount, and particle size distribution of inclusions at the outlet (submerged nozzle) of the refining vessel or continuous casting tundish. Using the deoxidation process simnlator, the macro behavior of nonmetallic inclusions in the tundish of a continuous caster at the Yawata Works were simulated and analyzed for coagulation and coalescence, flotation and removal, and advection and diffusion of nonmetallic inclusions in the refining vessel. The flotation and coagulation behavior of nonmetallic inclusions and the effect of dams and weirs on the flotation and coagulation behavior of nonmetallic inclusions are reported below.

4.1 Computational model

4.1.1 Enmeshment

For simplicity, the tundish is regarded as a rectangular parallelepiped. The x-, y-, and z-direction sides of the rectangular parallelepiped are divided into N_x, N_y, and N_z elements, respectively. In other words, the spatial elements $N_x \times N_y \times N_z$ are considered on the whole. Given its symmetry, one-fourth of the tundish is taken as the computational domain.

4.1.2 Coagulation and coalescence of inclusions

Concerning the coagulation and coalescence of inclusions in the tundish, Taniguchi and Kikuchi[13] expressed the collision frequency of particles in the turbulent field of the tundish by the following equation, quoting the equation of Saffman and Turner[14]:

$$N = 2(2\pi)^{1/2}R^2n_1n_2[1/2(1-\rho/\rho_p)^2(\tau_1-\tau_2)^2g^2 + (1-\rho/\rho_p)^2(dU/dt)^2+1/9R^2(\varepsilon/\nu)]^{1/2} \quad \cdots\cdots(3)$$

where N = collision frequency of particles of the diameters dp_1 and dp_2; R = $(dp_1 + dp_2)/2$; τ = particle relaxation time = $d_pr_p(18\mu)$; n_1 and n_2 = number density of particles 1 and 2, respectively; ρ and ρ_p = density of fluid and particles, respectively; ε = turbulent energy dissipation rate; ν = kinematic viscosity; μ = fluid viscosity; U = fluid velocity; and t = time.

In this model, the effect of coagulation due to Brownian motion is simultaneously taken into account by Eq. (4).

$$N' = \{n_1n_2(2kT)/(3\mu)\}(v_1^{-1/3} + v_2^{-1/3})(v_1^{1/3} + v_2^{1/3}) \quad \cdots\cdots(4)$$

where N' = collision frequency due to Brownian motion; k = Boltzmann's constant; v = volume of particles; T = absolute temperature

Eqs. (3) and (4) show the frequency of spherical particles colliding in a fluid. Take particles of alumina, for example, since alumina particles are solid, they do not always coalesce when

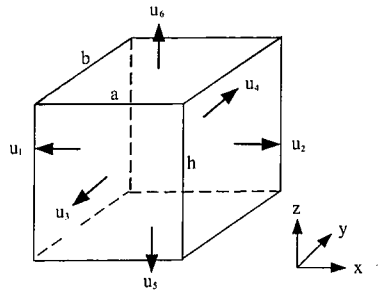

Fig. 12 Calculation of advection and diffusion of inclusions in each volume element

they collide. Even if they coalesce, they rarely become spherical, but often cluster. Since it is presently difficult to estimate the collision frequency of clustered particles, it is assumed here that particles that have collided and coalesced become spherical while retaining their volume. Furthermore, assuming that the collision probability of particles is constant, irrespective of their diameter, then by introducing the coalescence coefficient ξ, the coagulation frequency (NC) caused by collisions is defined as follows:

$$NC = \xi (N + N') \quad \cdots\cdots(5)$$

The coalescence coefficient ξ is such a constant that $0 < \xi < 1$, and its value is determined by adjnshing it to suit the actual situation.

4.1.3 Advection-diffusion and flotation of inclusions

As shown in **Fig. 12,** the amount of inclusions flowing out of each of the six faces comprising the spatial element per infinitesimal time unit is given by:

Bottom face

$$N_i = n_i(u_1 - u_{float})\Delta t/h \quad \cdots\cdots(6.1)$$

Top face

$$N_i = n_i(u_2 + u_{float})\Delta t/h \quad \cdots\cdots(6.2)$$

Side faces 1 and 2

$$N_i = n_i u_1 \Delta t/a,\ N_i = n_i u_2 \Delta t/a \quad \cdots\cdots(6.3)$$

Side faces 3 and 4

$$N_i = n_i u_3 \Delta t/b,\ N_i = n_i u_4 \Delta t/b \quad \cdots\cdots(6.4)$$

where N_i = number of particles of the diameter dp_i flowing out of each face; and u_{float} = flotation velocity of buoyant inclusions (relative to molten steel). The value of u_{float} is calculated by either of the following two equations, depending on whether the Reynolds number of particles, Re_p, is greater than one or not:

$Re_p < 1$: Alumina particle diameter $dp_i < 100$ μm

$$u_{float} = (2/9)g(dp_i/2)^2(\rho - \rho_p)/\mu \quad \cdots\cdots(7.1)$$

$Re_p > 1$: Alumina particle diameter $dp_i > 100$ μm

$$u_{float} = [4(\rho - \rho_p)^2 g^2/(225\mu\rho)]^{1/3} \quad \cdots\cdots(7.2)$$

4.1.4 Removal of inclusions

The removal of inclusions is divided into two cases. In one case, the inclusions are removed from the tundish after flotating to the surface of the molten steel. In the other, the inclusions are removed after colliding with the side or with the bottom refractory walls of the tundish. The present study considered the former case alone and ignored the latter. The removal rate of inclusions is basically calculated by Eq. (6.2). Since the surface of the molten steel in the tundish near the long nozzle is turbulent, the entrapment coefficient ζ is introduced to allow for the possibility of inclusions being entrapped again into the molten steel. Using the entrapment coefficient ζ, the number of inclusion particles of the diameter dp_i removed at the surface of the molten steel in the tundish is given by:

$$N_i = n_i u_{float} \Delta t(1 - \zeta)/h \quad \cdots\cdots(8)$$

where u_2 of Eq. (6.2) is not used because it is zero at the surface of the molten steel in the tundish. The entrapment coefficient ζ is greater than zero and defined as the ratio of the number of the inclusions that return to the molten steel without being removed from the total number of the inclusions that reach the surface of the molten steel in the tundish. In that sense, it should be rather called a flotation and removal impediment coefficient.

4.2 Computational results and discussion

The behavior of inclusions in the tundish of the No. 1 continuous slab caster at the Yawata Works was analyzed by this simulation method. The analyzed results were compared with the measured results of inclusions.

4.2.1 Flotation and removal behavior and coagulation behavior of inclusions

Tanaka et al.[15] counted the inclusions in aluminum-killed steel at the inlet and outlet of the tundish of the Yawata No. 1 continuous slab caster, and discussed the flotation and coagulation behavior of the inclusions according to their data. The removal ratio of inclusions calculated by the deoxidation process simulator when the tundish was provided with dams was compared with that measured by Tanaka et al. in **Fig. 13**. Assuming that there was no coagulation, the calculated values indicate that inclusions of 100 μm and larger are all removed from the molten steel in the tundish, a result that does not agree with the measured values of Tanaka et al. When coagulation is assumed to occur by putting the coalescence coefficient ξ at 1, inclusions of 50 μm and smaller grow by coagulation, are consumed, and sharply reduce in quantity. As a result, their removal ratio appears to be very large. When the coagulation and coalescence of inclusions were calculated by changing the coalescence coefficient ξ to 0.1, 0.3, and 0.5, the calculated values fall between those obtained when $\xi = 1$, and those obtained when the coagulation and coalescence of inclusions were not taken into account. Whatever the value of the coalescence coefficient ξ, the removal ratio of 50- to 100-μm inclusions slightly drops when their coagulation and coalescence alone are considered. Therefore, the measured values of Tanaka et al. cannot be explained by the data calculated by the deoxidation process simulator in this study.

Fig. 14 shows the removal ratio of inclusions calculated by fixing the coalescence coefficient ξ at 0.1, putting the entrapment coefficient ζ from the long nozzle to the first dam at 0.5, 0.7, or 0.9, and assuming no entrapment in other regions in the

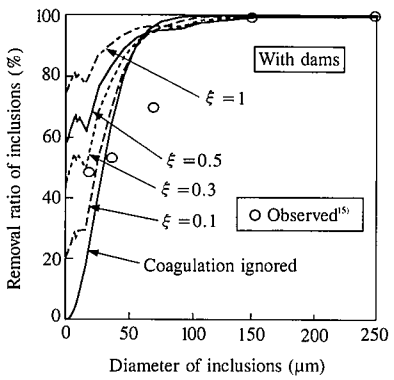

Fig. 13 Comparison of calculated and observed removal ratios of inclusions (ξ = 0, 0.1, 0.3, 0.5, 1, ζ = 0)

tundish. When $\zeta = 0.7$, the calculated results agreed well with the observed results. Concerning the coalescence coefficient ξ of alumina particles, Marechal et al.[16] reported a value of 0.03, while Taniguchi et al.[17] reported a value of 0.3 to 0.5. The value of 0.1 used in the present study to reproduce the inclusion counts of Tanaka et al. falls between the reported values. The entrapment coefficient of 0.7 suggests that a considerable amount of inclusions came from outside, probably due to the oxidation of the molten steel by entrapped tundish slag, or something present in the molten steel-slag interface exerted a very strong inhibiting effect on the flotation and removal of inclusions. The factor analysis of this point is currently under way.

To study which of the four coagulation mechanisms postulated has the largest effect on the removal of inclusions from molten steel in the tundish, the removal behavior of the inclusions was calculated by considering the coagulation rate of one mechanism alone and ignoring that of the other mechanisms. The calculated results are shown in **Fig. 15**. In this calculation, $\xi = 1$. As evident from **Fig. 15**, Stokes' coagulation mechanism is predominant in this case. The removal ratio curve according to Stokes' coagulation mechanism approximately agrees with that obtained when all of the four mechanisms are taken into account.

Taniguchi et al.[13] reported that the coagulation of inclusions in the tundish is controlled by the turbulent shear force of the molten steel. They estimated the turbulent energy dissipation rate ε at 10^{-1}, based on the fluid flow analytical results of Szekely et al.[18] In the actual tundish, the value of ε is large near the long nozzle and extremely small in the other regions, as shown in **Fig. 16**. This means that the turbulent shear mechanism is effective only in the vicinity of the long nozzle and that its effectiveness is small enough to be ignored as compared with Stokes' coagulation mechanism in the other regions of the tundish where the flow of the molten steel is mostly gentle.

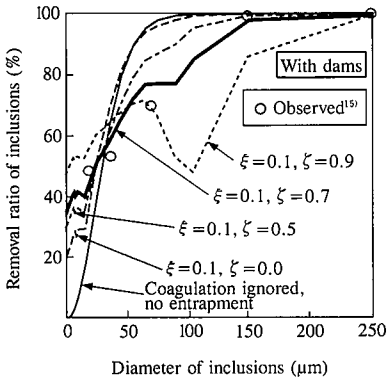

Fig. 14 Comparison of calculated and observed removal ratios of inclusions ($\xi = 0.1$, $\zeta = 0.3, 0.5, 0.7, 0.9$)

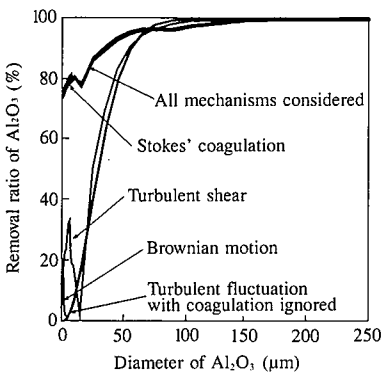

Fig. 15 Contribution of four coagulation mechanisms to removal ratio of nonmetallic inclusions

4.2.2 Effect of dams

In **Fig. 17**, the calculated removal ratio of inclusions in a tundish without dams is shown together with that in the same tundish with dams. The removal ratio of inclusions was calculated by assuming $\xi = 0.1$ and $\zeta = 0$. When the tundish was not dammed, the removal ratio of 50- to 150-μm inclusions alone was much smaller than when the tundish was dammed.

Figs. 18(a) and **18(b)** show the calculated particle size distributions of inclusions at the monitor points in the tundish (shown in **Fig. 19**), when the tundish was dammed and undammed, respectively. When the tundish was provided with dams, the amount of inclusions gradually decreased from the long nozzle toward the submerged nozzle. When the tundish was not provided with dams, the amount of inclusions at the outlet (position 7) was greater than at positions 5 and 6. These results can be explained without contradiction by regarding the outlet position as the terminal point of the preferential flow path for the molten steel in the tundish. To verify this assumption, the following calculation was performed. Inclusions in an amount 100 times greater than that present in a steady-state tundish were introduced through the long nozzle into the tundish (time 0). The change in the amount of inclusions flowing out of the outlet was then calculated.

The calculated results are shown in **Fig. 20**. When the tundish was dammed, the amount of inclusions leaving the outlet started to increase at about 4 minutes and reached the largest level at about 12 minutes. Since the capacity of the tundish is 60 tons, and the molten steel enters and leaves the tundish at a rate of 5 t/min, the average time to pass through the tundish was 12

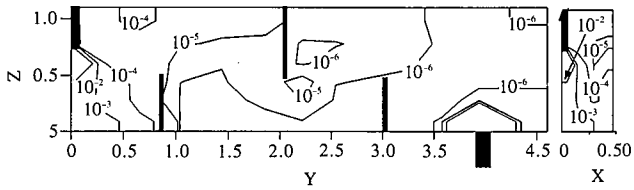

Fig. 16 Distribution of ε in tundish

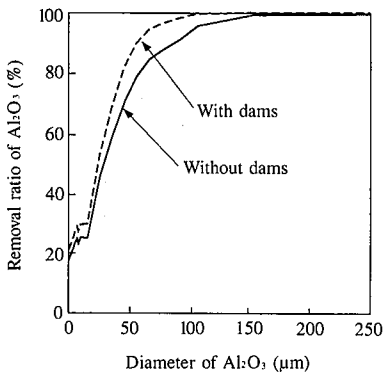

Fig. 17 Effect of dams on removal ratio of inclusions

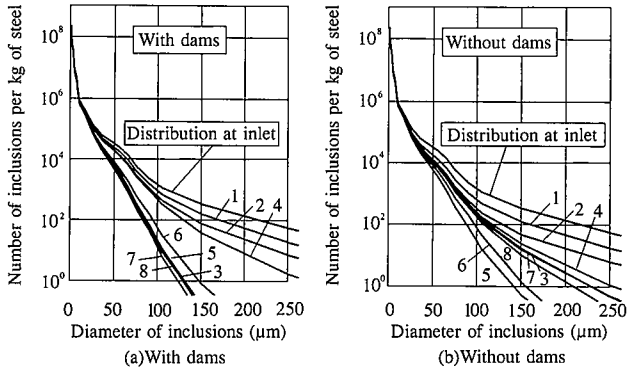

Fig. 18 Particle size distributions of inclusions in tundish with and without dams

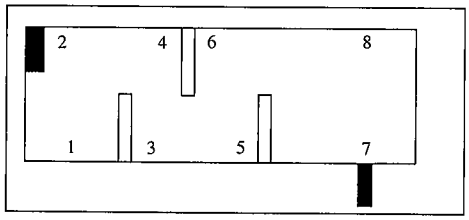

Fig. 19 Tundish positions of monitor points shown in Fig. 18

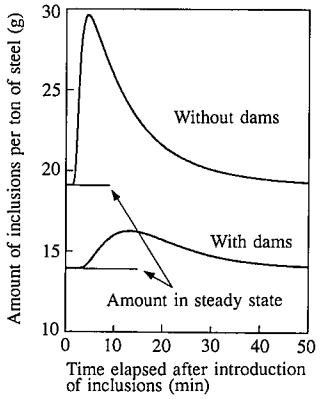

Fig. 20 Change in amount of nonmetallic inclusions at outlet when large amount of nonmetallic inclusions were introduced through inlet into tundish at time 0

minutes. The calculated results of **Fig. 20** indicate that when the tundish was dammed, the macroflow of the molten steel in the tundish is relatively uniform and that the inclusions follow the uniform macroflow path of the molten steel.

When the tundish was not dammed, the amount of inclusions flowing out starts to increase at about 2 minutes and reaches the largest level at about 4 minutes. In other words, the inclusions leave the tundish in about one-third of the average time taken by the molten steel to reach the outlet when the tundish is provided with dams. This means that when the tundish is not dammed, the molten steel nonuniformly flows in the tundish and that the inclusions reach the outlet in a short time by following the main flow path of the molten steel. This is also supported by the calculated streamlines of the molten steel in the tundish shown in **Fig. 21**.

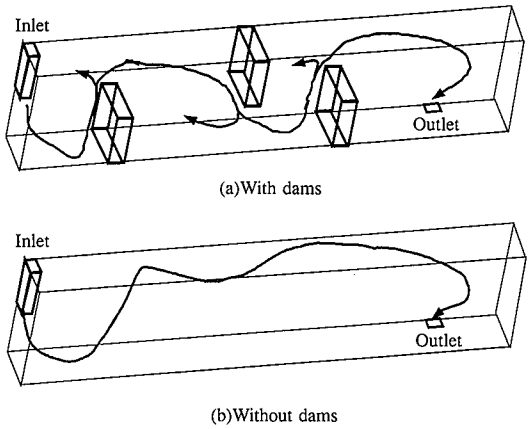

Fig. 21 Flow path of molten steel in tundish with and without dams

Conclusions

The complexity of the compositional control of nonmetallic inclusions makes it extremely difficult to find optimum values by experimental techniques alone for steels that must be controlled for a multiple-component system. This study has shown that computational thermodynamic techniques can be applied with great effectiveness in this field. Further work on the development of the deoxidation process simulator is expected to help accurately determine the amount and particle size distribution of nonmetallic inclusions and allow the strict control of nonmetallic inclusions in the steelmaking processes.

The authors believe that computational thermodynamics will certainly assume increasing importance in the field of inclusion control as it can fully utilize experimental data and drastically reduce the required number of experimental runs.

References

1) Gaye, H. et al.: Proc. of 4th Int. Conf. on Molten Slags and Fluxes. 1992, Sendai, ISIJ, p.103
2) Yamada, W. et al.: Shinnittetsu Giho. (342), 38 (1991)
3) Yamada, W. et al.: Proc. of the 6th International Iron and Steel Congress. Vol. I, 1990, Nagoya, ISIJ, p.618
4) Yamada, W. et al.: Proc. of International Conference on Computer-assisted Materials Design and Process Simulation. 1993, Tokyo, ISIJ, p.123
5) Sundman, B.: CALPHAD. 9, 153 (1985)
6) Hillert, M. et al.: CALPHAD. 14, 111 (1990)
7) Scheil, E.: Metallkd. 34, 70 (1942)
8) Clyne, T. et al.: Met. Trans. 12A, 865 (1981)
9) Easka, T. et al.: CAMP-ISIJ. 1, 268 (1988)
10) Hillert, M. et al.: Acta Chem. Scand. 24, 3611 (1970)
11) Pelton, A.D. et al.: Metall. Trans. 17A, 1211 (1986)
12) Kawauchi, Y. et al.: Private communication
13) Taniguchi, N., Kikuchi, J.: Tetsu-to-Hagané. 73, A211 (1987)
14) Saffman, P.G., Turner, J.S.: J. Fluid Mech. 1, 16 (1956)
15) Tanaka, H., et al.: Trans. ISIJ. 33, 1238 (1993)
16) Marcechal, L. et al.: Light Metals 1993. The Minerals, Metals & Materials Society, 1992, p.907
17) Taniguchi, N.: Private communication
18) Szekely, J. et al.: Steelmaking Processing. Vol.69,1986,Washington DC, p.761